

Nonlinear Elasticity of Microsphere Heaps

Carlos P. Ortiz, Karen E. Daniels, Robert Riehn

Dept. of Physics, North Carolina State University, Raleigh, NC, USA

(Dated: July 22, 2014)

Thermal fluctuations, geometric exclusion, and external driving all govern the mechanical response of dense particulate suspensions. Here, we measure the stress-strain response of quasi-two-dimensional flow-stabilized microsphere heaps in a regime in which all three effects are present using a microfluidic device. We observe that the elastic modulus and the mean interparticle separation of the heaps are tunable via the confining stress provided by the fluid flow. Furthermore, the measured stress-strain curves exhibit a universal nonlinear shape which can be predicted from a thermal van der Waals equation of state with excluded volume. This analysis indicates that many-body interactions contribute a significant fraction of the stress supported by the heap.

PACS numbers: 47.57.J-, 47.61.Jd, 05.40.Jc, 82.70.Dd

I. INTRODUCTION

The emergent mechanical properties of particulate matter play a central role in many physical processes and biological systems. Hard-sphere Brownian suspensions allow direct study of important condensed matter phenomena, such as the emergence of irreversibility from reversible equations of motion [1, 2], the glass transition [3–6], crystal nucleation and dislocation [7, 8], and dynamical heterogeneities [9, 10]. Both thermal fluctuations and geometric exclusion play significant roles in determining the bulk response of particulate matter, but little is known about the interplay between the effects. To probe this regime, we have developed a novel in-situ technique for measuring the elastic response of quasi-two-dimensional microsphere heaps confined by fluid stresses within a microfluidic device.

While the rheological properties of dense colloidal suspensions have been the subject of much study [12–24], and experiments show that elastic behavior dominates over viscous behavior on approach to a critical packing density [23, 25], much less is known about the solid-like properties of such systems above a rigidity transition. In this paper, we quantify the elastic response of very soft colloidal solids by varying the fluid stress on microsphere heaps assembled within a microfluidic channel [26]. This system is particularly suited to measuring the mechanical response of colloidal assemblies: the size and shape of the microsphere heap are direct observables, the relative contribution of fluid forces and thermal diffusion is tunable via the choice of particle size and fluid flow rate, and confining stresses from the fluid are applied as a bulk effect rather than from a single boundary. Inertial effects are negligible (thin film Reynolds number $Re \approx 10^{-8}$), and thermal and athermal effects are approximately equal in magnitude (Péclet number $Pe \gtrsim 1$). Here, we show that microsphere solids are more elastically-robust than ordinary solids, and their elastic modulus increases with the confining fluid stress. We observe that this family of solids is characterized by a universal nonlinear stress-strain curve, and we interpret this finding in light of a thermal equation of state [11].

II. EXPERIMENT

A. Apparatus

We use a microfluidic device to assemble microsphere heaps by flowing a dilute, aqueous suspension against a barrier (Fig. 1). The particles form a quasi-two-dimensional heap through gradual accumulation against a barrier, with the steady-state angle and size of the flow-stabilized solid set by the fluid flow rate [26].

Particles are deposited from a dilute suspension with mean two-dimensional areal density ρ , given by the number of microspheres per unit area, of $(110/(100 \mu\text{m})^2)$ against a flat-topped barrier. Due to the weak polydispersity of the particles, we observe polycrystalline domains within our heaps when they are examined with a higher-magnification objective. The device channel has a quasi-2D geometry with height $H = 1.8 d$, accommodating only a single layer of particles. The barrier is $h = 1.5 d$ high and occupies the center $w = 1000 d$ of a channel of width $W = 2000 d$, thus permitting flow around the top and sides of the barrier.

The aqueous suspension is composed of fluorescent polystyrene microspheres (530 nm, 5.9% polydispersity, elastic modulus ≈ 4 GPa), measured using dynamic light scattering (Malvern zetasizer) to have diameter $d = 530$ nm. We use steric and electrostatic stabilization (sulfate functionalized surface with ζ -potential of -60 mV and coated with Triton X-100) to provide reversible inter-particle and channel-particle interactions. The surfactant concentration was chosen to be small enough to avoid creating micelles, and this was confirmed using dynamic light scattering. Therefore, interparticle interactions beyond 2 nm are dominated by the electrostatic (DLVO) interaction.

For the experiments reported here, we prepare heaps under varying hydrodynamic confinement and record video of the heap size/shape due to changes in the applied pressure, from which we calculate the elastic bulk modulus K . We have prepared heaps under a variety of different barrier geometries, pH of the medium, and particle/channel ratios, and find that heap elasticity is a general phenomenon. In the experiments described below, we focus on a single set of parameters.

We control the suspension flow rate through the channel

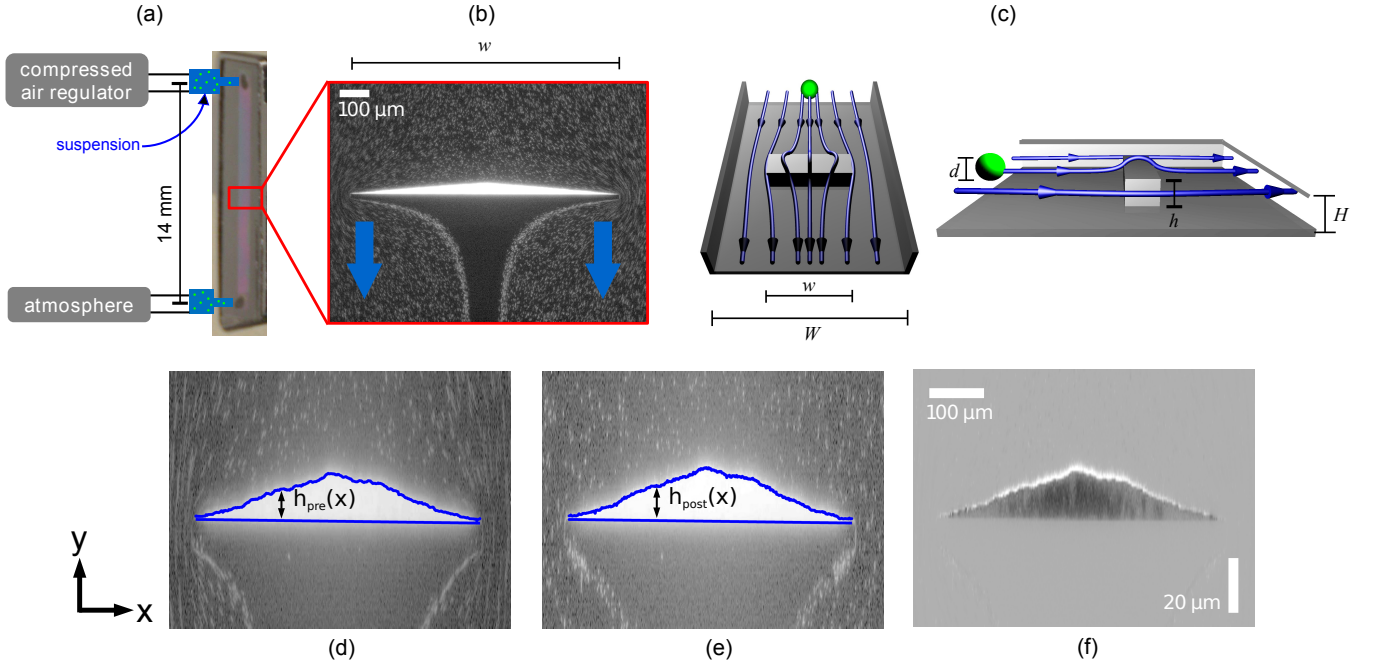


FIG. 1: Overview of Deformation Experiment. (a) Microfluidic experimental setup. (b) Grayscale fluorescence microscopy image depicting steady-state microsphere heap with suspension flowing around it. (c) Top-view and side-view diagram of Hele-Shaw microfluidic device geometry with fluid flow shown by blue streamlines. $W \times H \times L = 1 \text{ mm} \times 0.94 \text{ μm} \times 14 \text{ mm}$, not to scale), showing a single microsphere flowing towards the flat-topped barrier ($w \times h \times \ell = 563 \text{ μm} \times 0.84 \text{ μm} \times 10 \text{ μm}$). (a) Schematic microchip geometry. Steady-state raw fluorescence images (d) pre-perturbation and (e) 2.0 s after a perturbation of amplitude $\Delta P = -3.5 \text{ kPa}$. Linear grayscale represents fluorescence intensity, and blue line is the detected heap boundary. Fluid flow direction is from top to bottom. (f) Image-difference of the same sequence.

with a digital pressure regulator (AirCom PRE1-UA1) that applies pressurized air ($P_0 = 0 - 10 \text{ kPa}$ above atmosphere) to an o-ring sealed reservoir at the device inlet; the outlet is maintained at atmospheric pressure. We assemble heaps at steady pressures P_0 applied at the microchannel inlet such that $P_0 = 0 - 10 \text{ kPa}$ above atmospheric pressure. This pressure range includes the transition to stable heaps [26], and thus is the regime with the largest possible influence of thermal fluctuations. The corresponding Péclet numbers are between 4 and 28, which corresponds to observed heap angles of 1.3° to 5.4° . We deform the heap via a step change ΔP which, mediated by the flow rate, changes the fluid stress by an amount $\Delta\sigma \propto \Delta P$. We use a P to σ calibration curve developed using a Darcy flow model (see Appendix A). Using fluorescence microscopy, we visualize the deformation of the heap in response to the imposed $\Delta\sigma$ in real time. We chose wide-field fluorescence microscopy rather than confocal detection as this allows recording the fast dynamics of the entire system in real time. The light source is a continuous-wave Xenon lamp (X-cite 120); images of the fluorescence are collected with a Nikon Eclipse 80i fluorescence microscope with a $10\times$ Plan Fluor objective (N.A. 0.8) and an Andor Luca emCCD camera operating at 10 Hz frame rate.

To quantify the strain, we locate the boundary profile $h(x)$ of the heap by computing the gradient of the image along \hat{y} , then using a Gaussian fit to extract the heap profile. The pre- and post-deformation profiles $h_{\text{pre}}(x)$ and $h_{\text{post}}(x)$, provide a means to measure the local strain. As shown in Fig. 2, a para-

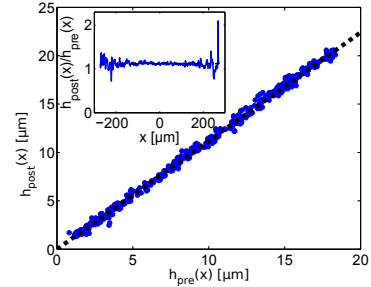


FIG. 2: Observation of uniform strain. (a) Parametric plot of $h_{\text{post}}(x)$ versus $h_{\text{pre}}(x)$ with inset local strain $\gamma(x) = h_{\text{post}}(x)/h_{\text{pre}}(x)$. In both plots, the dashed line corresponds to a mean strain of 12%, measured from the slope of (a).

metric plot of these two profiles is observed to be linear; this indicates that the deformation is well-described by a single mean strain. Equivalently, the ratio $h_{\text{post}}(x)/h_{\text{pre}}(x)$, shown in the inset, demonstrates that the strain is constant along the \hat{x} -direction. Therefore, we can use the change in area, ΔA , as a surrogate measure.

Since we are primarily interested in the elastic response, for which the timescale is $\approx 1 \text{ s}$, we are able to measure ΔA by taking the difference between two linear regressions to $A(t) = \int h(x, t) dx$, fit during the 3 s immediately before and after the deformation. This technique filters out any

slow drifts, and additionally allows measurements even when the deformation amplitudes are comparable to the background fluctuations. We tested the dependence of $\Delta A/A_0$ on its measurement early or late within the time-series and found no significant effect.

Figs. 1bc show sample pre- and post-deformation images; the difference image (Fig. 1d) shows a bright band of newly occupied volume that indicates an expansion of the heap. We locate the boundary profile of the heap via a Gaussian fit of the gradient in the y -direction. We find that applying a positive stress change $+\Delta\sigma$ leads to a compression of the heap in the y -direction. The resulting deformation is well-described by a single mean strain given by $\frac{\Delta A}{A_0}$, the ratio of the change in the size of the heap, ΔA , to the size of the heap prior to the deformation, A_0 (as shown in Fig. 2).

B. Inter-particle Separations

Due to the small size of the particles (530 nm) used in the experiment, it is not possible to optically resolve individual particles. Therefore, we perform a supplemental set of experiments in using a bidisperse 1:1 mixture of larger 600 nm and 710 nm particles ($H=1.32 d_g$) for which we could obtain particle positions. We use the larger diameter of 710 nm as the unit d_g in the following analysis and discussion. This steady-state pack is under $\sigma_0 = 0.1, 1.1$, or 3.9 Pa (corresponds to $P_0 = 0.1, 1$, or 7 kPa.) The pack is imaged with a $60\times$ water immersion objective (N.A. 1.00) and a $4\times$ beam expander. We compute a mean image by taking the average over a small set of images, each with a 0.1 s exposure time, for a 1.0 s integration time. We use a Wiener deconvolution algorithm with a Gaussian point spread function to process the raw fluorescence images and find the particle positions. Particles are detected in the deconvolved image by searching for local maxima that are connected bright pixels of a threshold value relative to their environment. For each local maxima region, we find a centroid that corresponds to the most probable particle position. These centroids are shown as black crosses overlaid over the raw image in Fig. 3a. We determine the accuracy of the algorithm on synthetic images with known particle centers and radii, subject to simulated Poisson noise and optical blurring. Using Wiener deconvolution, we are able to recover the position of the particles to $0.05 d_g$. We detect no pixel-biasing in either the results from synthetic or the real images. From the centroids, we compute $g(r)$ from the normalized histogram of the interparticle pairwise distances. Each $g(r)$ curve in Fig. 3 contains more than 500,000 particle positions.

From a parabolic fit for separations from $0.9 d_g$ to $1.2 d_g$, we find that the position of the nearest-neighbor peak in $g(r)$ is $(1.09 \pm 0.02) d_g$ for a confining stress of 0.1 Pa. Increasing the confining stress reduces the interparticle separation, as shown in Fig. 3c. Using the simulated images, we find errors in the particle positions do not systematically bias the peak position in $g(r)$ relative to the true position; the absolute standard error in the peak position is $0.02 d_g$, while the uncertainty is $0.03 d_g$. The trend in Fig. 3cd is larger than these errors. In

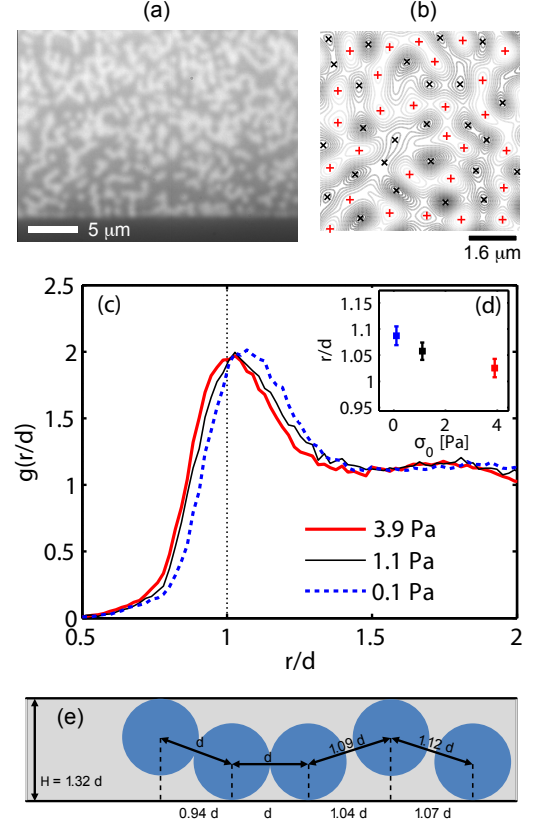


FIG. 3: (a) Fluorescence microscopy image of a microsphere heap composed of bidisperse particles under steady confining stress $\sigma_0 = 0.1$ Pa. Diameter of dim particles is 600 nm and of bright particles is 710 nm. (b) Intensity contour lines showing particle centroids in microsphere heap, detected using Wiener deconvolution. Light contours with + (red) correspond to bright regions, and dark contours with \times (black) correspond to dim regions. (c) Pair radial distribution functions, $g(r/d)$, measured at three different σ_0 : 0.1 Pa, 1.1 Pa, 3.9 Pa. (d) Peak position as a function of the confining stress σ_0 , measured from a parabolic fit to the peak, with $1-\sigma$ (68.3 %) confidence intervals. (e) Schematic of possible configurations of microspheres in the channel and their apparent separations when observed from above.

addition, we have verified that these results are robust to small changes in the image processing parameters and pair distribution algorithm parameters. The significance of this result is that most of the nearest neighbors are found 9% farther than 1 particle diameter, and are thus not true contacts in the Hertzian sense. Our finding is strengthened by the observation that $g(r)$ is confining-stress dependent, which would not be anticipated for a Hertzian contact network. Finally, d_g is larger than the average particle diameter, and so the first peak in $g(r)$ would actually be larger if it were in units of the average particle diameter.

Our observation of non-zero $g(r)$ below $1.0 d_g$ suggests a fraction of particle configurations with either intimate surface contact or staggered out-of-plane positions. Fig. 3e shows schematic of the influence on $g(r)$ of microsphere configurations in a microchannel of $H = 1.32 d_g$. Apparent separa-

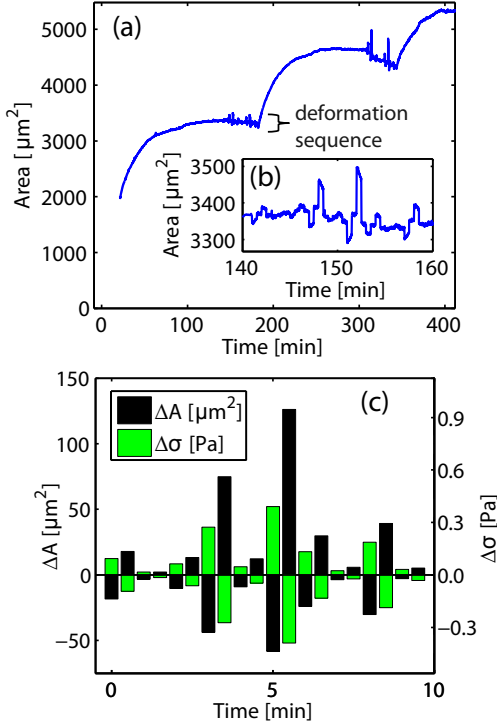


FIG. 4: Stress-Strain Measurement Protocol. (a) Heap growth to steady state at $P_0 = 1$ kPa ($\sigma_0 = 0.7$ Pa) during two hours of particle accumulation, followed by a sequence of 80 randomized deformations, and then repeated for a larger value of $P_0 = 2$ kPa. (b) Inset: Zoom of $A(t)$, for which the extracted values of ΔA (black) and $\Delta\sigma$ (green) are shown in (c).

rations below $1.0 d_g$ are possible due to staggered configurations with intimate surface contacts and that apparent separations of $1.07 d_g$ could indicate interparticle separations as large as $1.12 d_g$.

III. RESULTS

We measure the elastic response for heaps formed at seven different initial stresses ($\sigma_0 = 0.1$ to 4 Pa). Fig. 4a illustrates the time-evolution of A for the first two values of σ_0 . At time $t = 0$, the suspension is released into the microchannel and over 2 hours the heap size grows to its steady state at A_0 . This value is σ_0 -dependent, and was previously attributed to a critical Péclet number [26]. A series of deformation experiments is then performed on the steady-state heap; this process is repeated for increasing values of σ_0 , each of which is allowed to reach a steady state.

The series of deformation cycles on each heap is an identical randomized set of 80 logarithmically-spaced values of $\Delta\sigma$ from 2 mPa to 3.8 Pa. For each $\Delta\sigma$, the cycle contains four deformations around σ_0 ($+\Delta\sigma, -\Delta\sigma, -\Delta\sigma, +\Delta\sigma$); overall the full series comprises 320 deformations. Fig. 4b shows a detailed view of this sequence, and Fig. 4c shows the measured values of $(\Delta\sigma, \Delta A)$ extracted from the sequence. As is ex-

pected for an elastic response, an increase (decrease) in σ corresponds to an decrease (increase) in A . Each pair of such measurements provides a point along the stress-strain curve at that value of σ_0 .

We find that large-scale expansions lead to some shedding of particles, which leads to lower A after the deformation. The erosion process is facilitated by the fluidization of particles at the heap interface [26]. Because re-deposition of particles is slower than the timescale of the experiments, we observe an apparent slight shrinking of the heap during a deformation sequence, as shown in the second deformation series in Fig. 4a. While randomizing the sequence minimizes the impact of memory effects ΔA vs. $\Delta\sigma$ relationship, the erosion complicates the measurements for small $\Delta\sigma$ late in the sequence. To account for this effect, we define the effective heap size A_0 for each step immediately before the deformation step rather than the initial steady state area.

A. Deformations

We present the stress-strain curves for the full set of experiments in Fig. 5a. Near $\Delta\sigma = 0$, we find an approximately linear response for all steady-state heaps, as shown in Fig. 5b. At large deformations, a nonlinear relationship becomes apparent, but is nonetheless still reversible. For each curve, we measure the linear elastic modulus K by linearizing around $\Delta\sigma = 0$:

$$\frac{\Delta A}{A_0} = -\frac{\Delta\sigma}{K} \quad (1)$$

over the range $|\Delta A/A_0| < 0.015$. The magnitude of K determined here is consistent with the literature for crystallized sub-micron colloidal polystyrene [27] or silica [28–30] particles. The observation of a large elastic regime (up to 10%-15% strain), stands in contrast to ordinary solids in which such strains would cause fracture.

As shown in Fig. 5c, we find that flow-stabilized solids formed under higher compression (larger σ_0) are stiffer (larger K). This is unlike ordinary solids, where K is a constant for small compressions, and suggests that the elastic response is controlled by the steady state stress σ_0 . We observe an approximately linear relationship between K and σ_0 , with

$$K = \alpha \sigma_0. \quad (2)$$

where α is the compressibility factor. Because Eqns. 1 and 2 together imply $\frac{\Delta A}{A_0} \propto \frac{\Delta\sigma}{\sigma_0}$ for small deformations, we seek to collapse all of the stress-strain measurements onto a single curve. In Fig. 6a, we test whether this dependence extends to larger deformations by rescaling $\Delta\sigma$ by σ_0 . In Fig. 6b, we observe that the linear approximation extends for two orders of magnitude in strain, with increasing scatter below $\Delta A/A_0 \approx 0.02$ and deviations in decompression above $\Delta A/A_0 \approx 0.3$. The extent of this data collapse, well beyond the linear regime which motivated it, suggests a deeper connection between the stress and strain which we explore below.

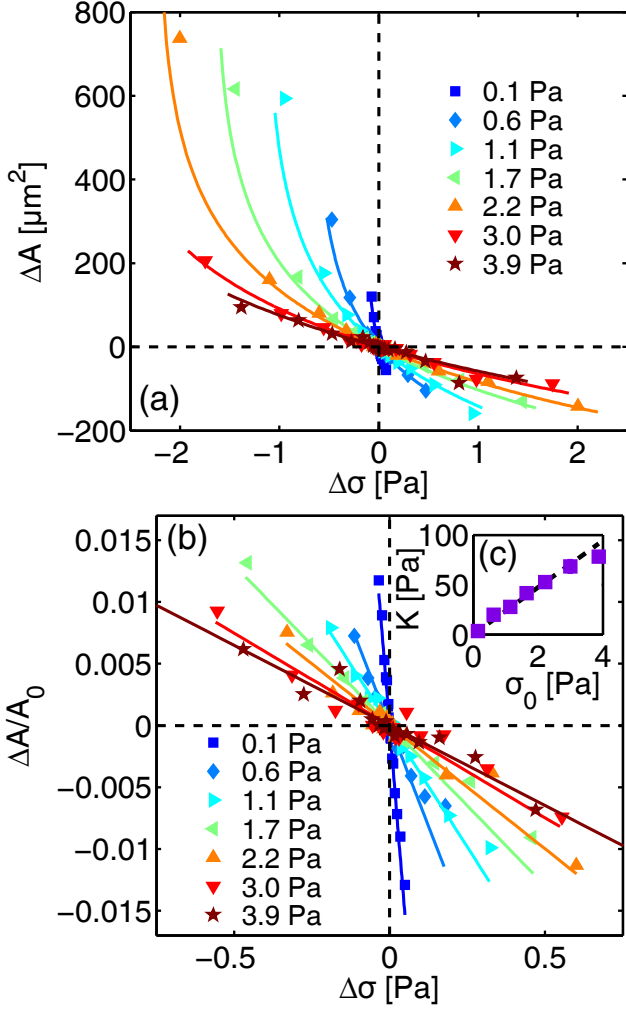


FIG. 5: Raw stress-strain measurements. (a) Scatter plot of perturbation amplitude $\Delta\sigma$ vs. deformation amplitude ΔA for seven difference values of σ_0 indicated by symbol shape. Lines are fits to Eq. 10. The measurement range is largest at intermediate values of σ_0 , truncated for small values by the lower limit of heap formation at $\text{Pe} \approx 2$ [26] and at large values by the pressure regulator. (b) Stress-strain measurements for the same data. Each line is a linear fit to determine the elastic modulus K (see Eq. 1). (c) Inset: Measured values of K from (b) as a function of σ_0 , with error bars indicating one standard deviation estimates obtained from the fits. The dashed line is the linear fit is to Eq. 2 with $\alpha = 23.3 \pm 0.74$.

IV. DISCUSSION

In order to explain the observed universal, nonlinear elastic response, it is reasonable to consider either thermal (classical, hard-sphere equation of state [35, 36]) or athermal (jamming [37, 38]) theories. In these experiments, we observe that because the particles are both immersed in a fluid and subject to thermal fluctuations, they exhibit diffusive motion and are not typically in contact with each other. As shown in Section §II B, we estimate that less than 20% of interparticle contacts are close enough for direct contact to be possible. A movie

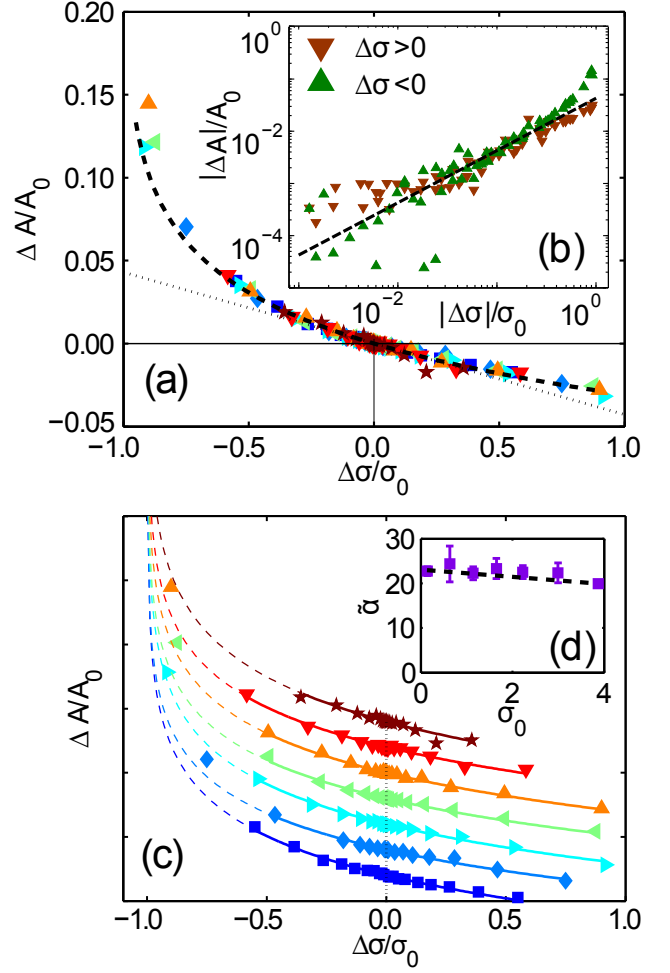


FIG. 6: Scaled stress-strain measurements. (a) Strain $\Delta A/A_0$ as a function of the scaled perturbation amplitude $\Delta\sigma/\sigma_0$, showing data collapse. Dashed solid line is from Eq. 10 with $\tilde{\alpha} = 22.5$; thin dotted line is Eq. 1 with $K = \alpha\sigma_0$ and $\alpha = 23.3$. Symbol legend is the same as in Fig. 5. (b) Inset: Log-log plot of $\Delta A/A_0$ versus $|\Delta\sigma|/\sigma_0$ where compressions are upward (green) triangles and decompressions are downward (brown) triangles. Dashed solid line is Eq. 1 with $K = \alpha\sigma_0$ and $\alpha = 23.3$. (c) The same data, with the curves vertically shifted by 0.1 to allow for comparison. Each curve is fit to Eq. 10 to find a best-fit value of $\tilde{\alpha}$; solid lines denote the fit region and the dashed lines are continuations beyond that region. (d) Inset: Values of $\tilde{\alpha}$ for each dashed curve fit in (c). Error bars are one standard deviation parameter variance estimates for each regression obtained from adding the parameter variance from the Hessian of the error function and systematic errors. Dashed line is a linear fit: $\tilde{\alpha} = (23.4 \pm 2.3) + (-0.24 \pm 0.17)\sigma_0$.

showing the thermal rearrangements in the center of the heap is included as Supplemental Data.

The nondimensional number typically used to quantify the transition from thermal to athermal behavior is the Péclet number Pe , calculated as the ratio of the particle self-diffusion time $\tau_D = d^2/D$ to the particle advection time $\tau_a = d/v$. In previous work [26], we found that the Péclet number at the heap interface, $\text{Pe}_\infty = \frac{dv_\infty}{D_\infty}$, is a good predictor for the for-

mation of a microsphere heap from a dilute suspension. For the 530 nm spheres, we find D_∞ to be $0.55 \mu\text{m}^2/\text{s}$ from the slope of the long-time mean-squared displacement of microspheres in the absence of external driving, and we measure v_∞ from the streamline bounding the heap. We calculate that the heaps in this paper probe the range Pe_∞ from 4 to 28. In fact, these above-unity values represent an upper bound for the local Péclet number. Within the heap, Pe would be better estimated by the advection time due to the local shear rate $\dot{\gamma}(\phi, y_\perp)$, which depends on both the distance y_\perp into the heap and the packing fraction ϕ . Therefore, the local Péclet number $\text{Pe}(\phi, y_\perp) = \frac{d^2 \dot{\gamma}(\phi, y_\perp)}{D(\phi, y_\perp)}$. Due to hydrodynamic screening, it is likely that an exponential decay in the local shear rate [31–33] causes a similar decay in the local Pe . This effect would dominate the presumed algebraic decay of the self-diffusion constant (due to the growth of the shear viscosity at large packing fractions [12, 34]). Therefore, local values of Pe are smaller than estimates from Pe_∞ , likely unity or below. Future studies that measure the self-diffusion constant in the interior of the heap would allow for direct probes of the thermal-athermal transition.

Therefore, we consider the system only in a thermal context, starting from the van der Waals equation of state $p(A - A_c) = Nk_B T$ [11], where p is the pressure and A_c is the smallest area that the system can achieve without particle overlap and A is the area occupied by the heap (including interstitial volume). This equation of state is limited to situations where the shape of the accessible volume is invariant under deformations, and cage-breaking [39] is unlikely. Because the degrees of freedom attributed to the particles within an aqueous suspension do not contribute significantly to the heat capacity, we also assume that our experiment is performed isothermally. Note that the applicability of the van der Waals equation of state to driven granular systems has previously been observed in both simulations [40] and experiments [41].

We consider the 2D isothermal deformation of a pack of disks subject to the van der Waals equation of state:

$$\sigma(A - A_c) = C = \text{constant} \quad (3)$$

where σ is the stress, A is the area occupied by the material, A_c is the excluded area due to the size of the particles such that $A \geq A_c$. A total differential of Eq. 3 gives:

$$\frac{d\sigma}{dA} = -\frac{\sigma}{A - A_c} \quad (4)$$

The bulk modulus $K = -A \frac{d\sigma}{dA}$ is

$$K = \frac{\sigma}{1 - \frac{A_c}{A}} \quad (5)$$

In a material composed of monodisperse particles, the packing fraction $\phi \equiv \frac{NA_1}{A}$, where N is the number of disks, A_1 is the cross-sectional area of a single particle. Then, $\frac{A_c}{A} = \frac{\phi}{\phi_c}$, where ϕ_c is the densest possible packing fraction. Based on our observations in Fig. 3, we define α by Eq. 2 of the main text as

$$K = \alpha \sigma_0. \quad (6)$$

Combining Eqns. 5 and 6 allows the identification

$$\alpha = \frac{1}{1 - \frac{A_c}{A}}. \quad (7)$$

To find the stress-strain relation, we consider two instances of Eq. 3, at steady state (σ_0, A_0) and after deformation $(\sigma_0 + \Delta\sigma, A_0 + \Delta A)$:

$$\sigma_0(A_0 - A_c) = C \quad (8)$$

$$(\sigma_0 + \Delta\sigma)(A_0 + \Delta A - A_c) = C \quad (9)$$

Taking the ratio of Eq. 9 and Eq. 8 eliminates the unknown constant C . Solving for $\frac{\Delta A}{A_0}$ gives

$$\frac{\Delta A}{A_0} = \left(1 - \frac{A_c}{A_0}\right) \left(\frac{1}{1 + \frac{\Delta\sigma}{\sigma_0}} - 1\right) \quad (10)$$

Identifying the factor $\left(1 - \frac{A_c}{A_0}\right)$ as $1/\alpha$ simplifies the expression to:

$$\frac{\Delta A}{A_0} = \frac{1}{\alpha} \left(\frac{1}{1 + \frac{\Delta\sigma}{\sigma_0}} - 1\right), \quad (11)$$

which we use for making fits to the data. We denote α as the fit parameter to Eq. 6, and $\tilde{\alpha}$ as the fit parameter to Eq. 11.

To test the agreement between this function and Fig. 6a, we individually fit each of the seven stress-strain curves to Eq. 11 and take the compressibility factor $\tilde{\alpha}$ as a free parameter. We note that α and $\tilde{\alpha}$ could possibly differ as one is a constant arising from the geometry, and the other is a fitting parameter to experimental data. The resulting seven curves are shown in Fig. 6c, with the fit values of $\tilde{\alpha}$ provided in the inset. We find that Eq. 11 is in good agreement with all compressive data and small decompressions, while large decompressions ($\Delta\sigma/\sigma_0 \lesssim -0.7$) deviate significantly. Furthermore, the values of $\tilde{\alpha}$ obtained in the fits are in agreement with the one obtained in the linearized data (Fig. 5c), indicating we have achieved a valid measurement of the compressibility factor. The magnitude of this compressibility factor indicates significant deviation from ideal gas behavior, where $\alpha \sim \mathcal{O}(1)$. Expressing the compressibility factor as a virial cluster expansion of packing fraction ϕ gives $\alpha = 1 + \sum_{i=1}^{\infty} B_{i+1} \phi^i$. Comparing our measured α to the known virial expansion coefficients [46] indicates the expansion must include terms of at least fifth order. This observation implies that the elastic process measured by the compressibility is subject to significant contributions from many-body interactions. In addition, we observe that $\tilde{\alpha}$ decreases slightly with increasing σ_0 . This may be associated with a stress-dependent packing fraction, an idea which is supported by Fig. 3cd and Appendix A.

V. CONCLUSIONS

The agreement between our observations and the stress-strain relation derived from a simple thermal (van der Waals)

equation of state is an encouraging first-step for building more general physical models in this important regime where the Péclet number is close to unity. This finding highlights the importance of geometric exclusion in setting the material properties of particulate matter. We have shown that microsphere heaps support external stress by measuring their bulk modulus. We have further shown that this stress is supported by the particle network via a mechanism involving many-body particle interactions. A direct measurement of the particle positions during deformation would allow for a more detailed understanding of the microscopic origins of the stress-strain relation. The reversibility of the elastic response opens new possibilities for the manipulation of cells and droplets in microfluidic devices, including the design and assembly of new material.

VI. ACKNOWLEDGEMENTS

We are grateful for support from the National Science Foundation through an NSF Graduate Fellowship, and grants DMR-0644743 and DMS-0968258. This work was performed in part at the Cornell NanoScale Facility, a member of the National Nanotechnology Infrastructure Network, which is supported by the National Science Foundation (Grant ECCS-0335765). This work was also performed in part at North Carolina State University facilities: Nanofabrication Facility, Advanced Instrumentation Facility, and Education and Research Laboratory.

Appendix A: Flow Model

This section describes the flow model we use to determine the stress σ_0 supported by the microsphere heap, as a function of P_0 , the pressure applied at the microchannel inlet. The model is motivated by the observation that there exists an excluded zone downstream of the barrier, into which particles do not flow (see Fig. 7). This excluded zone is formed by liquid which has flowed through the heap and barrier. Given knowledge of the channel dimensions, we find that the asymptotic width (ξ) of this zone measured far downstream of the barrier, together with the flow velocity measured far upstream of the barrier, provides a measure of both the flow rates around and through the heap/barrier, and the applied stress on the heap.

In making this calibration, we assume that the flow is laminar, and is plug-like along the x -direction far away from the heap. Following [42], we calculate the thin-film Reynolds number from the channel geometry and maximum fluid speed ($U = 100 \mu\text{m/s}$) as $Re = \frac{\rho UL}{\eta} \left(\frac{H}{L}\right)^2 \approx \mathcal{O}(10^{-8})$, with ρ the density and η the viscosity, validating the assumption of laminar flow. We model the fluid flow within the microchannel using Stokes' equation $\eta \nabla^2 \vec{u} = \nabla p$, where p is the pressure, and the incompressibility condition $\nabla \cdot \vec{u} = 0$. We numerically verify that the flow within the microchannel without heap and barrier deviates by less than 10% from a plug-like flow in the (x, y) -plane except within two particle diameters from the side walls (similar to [44]). We neglect the

z -direction, where we expect Poiseuille flow in microchannel areas without a heap, and plug-like flow within the heap due to Darcy's law.

The flow everywhere in the xy -plane can therefore be modeled in a fashion similar to Darcy flow since the viscous stresses in the z -directions are far larger than those in the x and y directions within the microchannel. We solve the two-dimensional Laplace equation for the pressure, $\nabla \cdot [\kappa(x, y) \nabla p] = 0$ using the MATLAB PDEtool. The local permeability κ is chosen such that the fluid volume flux $\vec{v}(x, y) = -\frac{\kappa}{\eta} \nabla p(x, y)$ agrees with experimental streamline observations. $\vec{v}(x, y)$ models the mean liquid velocity in the microchannel regions. We solve the two-dimensional Laplace's equation for the pressure. Each of three regions of space (barrier, heap, free channel) is assigned a constant value of κ (κ_{bar} , κ_{heap} , κ_{dev} , respectively). A sample such solution is shown in Fig. 8a.

Using the pressure distribution $p(x, y)$ within the channel, we obtain streamlines of constant $\psi(x, y)$ satisfying $\vec{v}(x, y) = \left(\frac{\partial \psi(x, y)}{\partial y}, -\frac{\partial \psi(x, y)}{\partial x} \right)$. We are particularly interested in the streamlines touching the left and right edges of the barrier, labeled ψ_L and ψ_R in Fig. 7e, respectively, as these two streamlines form the boundaries of the excluded zone. Particles from streamlines that intersect the barrier are either added to the heap or travel along the edge of the surface until they flow off the surface of the heap at the ends of the barrier. Thus, they follow the pair of streamlines from the ends of the barrier, and leave a particle-free (excluded) zone at the center of the flow. Note that, at finite Pe , particle diffusion does allow some particles to cross streamlines and enter this zone.

Downstream of the barrier, ψ_L and ψ_R asymptote to a lateral separation distance ξ as the plug-like flow is restored where streamlines are parallel, and the volume flux \vec{v} is independent of x . We find the ratio of flow rates through the heap/barrier (Q_{heap}) and the total flow volume through the device (Q_{∞}) via a ratio of the widths of the excluded zone and the entire device: $\frac{Q_{\text{heap}}}{Q_{\infty}} = \frac{\xi}{W}$. In the following, we match simulated shapes of Ψ_L and Ψ_R to the experimentally obtained shape of the excluded zone. To determine the average flow velocity upstream of the barrier, we measure the peak of the spatial cross-correlation of particle trajectories in adjacent frames. Q_{∞} is then determined from the particle velocity far upstream from the heap, as is the pressure gradient far away from the heap.

We first compare simulation and experiment for a device in the absence of a heap on the barrier. The analytic expression for the relative permeability of the barrier is $\frac{\kappa_{\text{bar}}}{\kappa_{\text{dev}}} = \left(1 - \frac{h}{H}\right)^2$, where h is the height of the barrier within the channel of height H (both in the z -direction). Fig. 8b shows the simulated ξ_0/w as a function of h/H . We measured $h = 0.84 \mu\text{m}$ and $H = 0.94 \mu\text{m}$ for our device. The flow shapes in experiment and theory closely resemble each other, and we find that our measured ξ_0/w agrees with the simulated ξ_0/w for our measured h/H in Fig. 8b.

For devices with heaps, we adjusted κ_{heap} to yield a simulated flow profile equal to that observed in experiments while

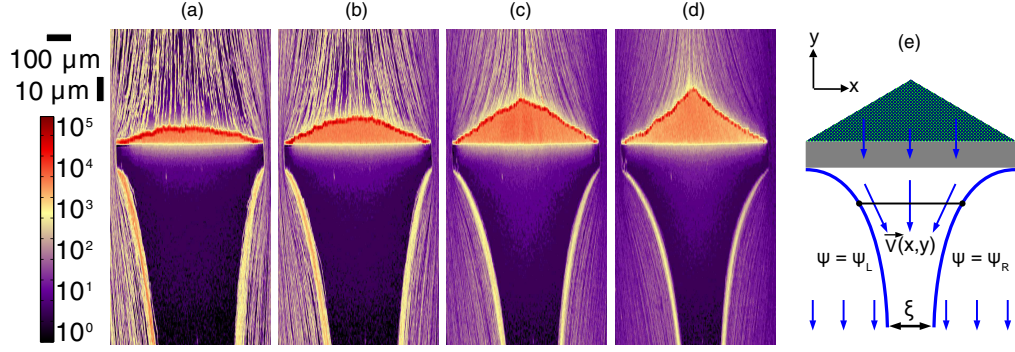


FIG. 7: (a-d) Processed images showing amplitude of intensity fluctuations at different inflow velocities. Each pixel is given an RGB color proportional to the standard deviation measured over 8 s (80 images) after steady state was reached. The colormap is reported in arbitrary units, with purple indicating low fluctuations and red indicating high fluctuations. The large purple areas are the excluded zones. Tracks of single particles are yellow trails. The strongly fluctuating (fluid-like) areas at the surface of each heap are deep red, while the weakly fluctuating (solid-like) interior of the heap is light red. From left to right, the inflow velocities are 3.6 $\mu\text{m/s}$, 7.1 $\mu\text{m/s}$, 14.2 $\mu\text{m/s}$, 35.5 $\mu\text{m/s}$. Microsphere areal density far from the heap is constant $\rho_\infty = 110/(100 \mu\text{m})^2$. (e) Schematic drawing showing streamlines ψ_L and ψ_R bounding the excluded zone of width ξ .

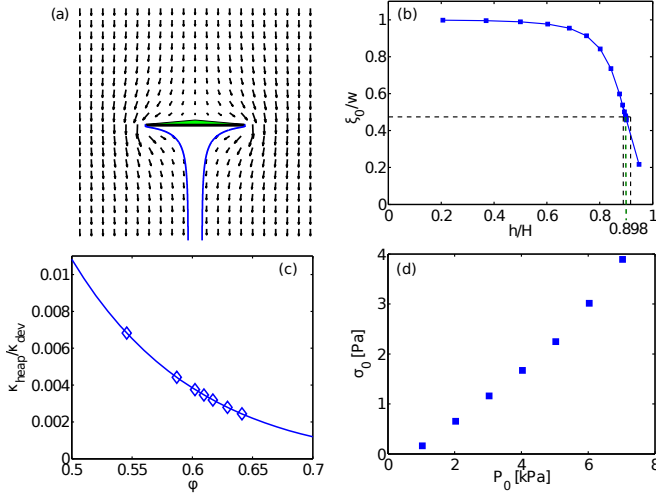


FIG. 8: (a) Simulated depth-averaged velocity field. The two solid lines are the streamlines that define ξ . (b) Solid line shows plot of ξ_0/w in simulation versus the value of h/H . Dashed lines show the range of experimental measurements of h/H and ξ_0/w . (c) Simulated relative heap permeability versus heap packing fraction ϕ at 7 values of P_0 (left is low P_0 , right is high). Solid line given by Eq. A1. (d) Final calibration of σ_0 (pressure on heap surface calculated by Eq. A2) as a function imposed pressure P_0 for each of the 7 experimental conditions.

maintaining the ratio of $\kappa_{\text{bar}}/\kappa_{\text{dev}}$ obtained from Fig. 8b and a shape of the heap that is observed in experiments. We find that κ_{heap} is lower for heaps assembled at higher steady-state stresses, and higher for assembly at low stresses. However, we had to assume a uniform κ_{heap} for the heap at each flow condition due to the insufficient information on stream lines within the heap. In view of the position-independent strain described in the previous section, this choice appears not to be problematic.

We now compare the permeabilities obtained from the combination of experiment and numerical model to those

predicted by the Carman-Kozeny model for a collection of spheres of packing fraction $\phi \equiv \frac{V_{\text{spheres}}}{V_{\text{total}}}$ ([43, 45]). Given $\kappa_{\text{dev}} \approx \frac{1}{12}H^2$, the Carman-Kozeny relation relates the permeability of the heap to its packing fraction ϕ :

$$\frac{\kappa_{\text{heap}}}{\kappa_{\text{dev}}} = \frac{(1-\phi)^3}{\phi^2} \frac{d^2}{180} \frac{12}{H^2} \quad (\text{A1})$$

The solid line in Fig. 8c corresponds to the Carman-Kozeny permeability at a given apparent packing fraction. Note, these apparent packing fractions are not confirmed by direct measurements, only inferred from the model. The apparent packing fractions are in the range 0.54 to 0.64, although we note that the nearly 2-dimensional packing renders the void volume of a different shape that the 3-dimensional Carman-Kozeny system. Importantly, Fig. 8c highlights the need for detailed structural information to better understand the nature of the rigidity, because the stress supported by the heap depends on this coupling between its packing fraction and its permeability.

Using our experimentally-determined permeabilities, we use the full solution of the Laplace equation to determine the fluid stress on the heap, without needing specify the local packing fractions. Inspection of the data set shows that the flow velocity within heap and barrier is approximately in the y -direction. Together with the incompressibility of the liquid, this implies that the flow velocity through barrier is well-defined as a function of only x . Since the observable chosen for the deformation is the area, we identify the fluid stress as the area-averaged stress formed by

$$\sigma = \frac{1}{A} \int_{-w/2}^{w/2} (p(x, y_{\text{surr}}(x)) - p(x, y_{\text{bott}})) (y_{\text{surr}}(x) - y_{\text{bott}}) dx. \quad (\text{A2})$$

Here $y_{\text{surr}}(x)$ is the location of the upstream surface of the heap, and y_{bott} is the location of the interface between heap and barrier. The resulting calibration curve for all data in this publication is shown in Fig. 8d.

-
- [1] L. Cort , P. M. Chaikin, J. P. Gollub, and D. J. Pine, Nat. Phys. **4**, 420 (2008).
 - [2] D. J. Pine, J. P. Gollub, J. F. Brady, and A. M. Leshansky, Nature **438**, 997 (2005).
 - [3] E. R. Weeks, Science **287**, 627 (2000).
 - [4] A. Yethiraj and A. van Blaaderen, Nature **421**, 513 (2003).
 - [5] P. Ballesta, R. Besseling, L. Isa, G. Petekidis, and W. Poon, Phys. Rev. Lett. **101**, 1 (2008).
 - [6] G. L. Hunter and E. R. Weeks, Reports Prog. Physics. **75**, 066501 (2012).
 - [7] D. R. Nelson and B. I. Halperin, Phys. Rev. B **19**2457 (1979).
 - [8] P. Schall, I. Cohen, D. A. Weitz, and F. Spaepen, Nature **440**, 319 (2006).
 - [9] A. R. Abate, H. Katsuragi, and D. J. Durian, Phys. Rev. E **76**, 061301 (2007).
 - [10] K. N. Nordstrom, J. P. Gollub, and D. J. Durian, Phys. Rev. E **84**, 021403 (2011), 1103.2357.
 - [11] J. D. van der Waals, Ph.D. thesis, Leiden University (1873); J. Clerk Maxwell, Nature **10**, 477 (1874).
 - [12] I. M. Krieger, Adv. Colloid Interface Sci. **3**, 111 (1972).
 - [13] C. G. de Kruif, E. M. F. van Iersel, A. Vrij, and W. B. Russel, J. Chem. Phys. **83**, 4717 (1985).
 - [14] J. C. van der Werff, C. G. de Kruif, C. Blom, and J. Mellema, Phys. Rev. A **39**, 795 (1989).
 - [15] P. N. Segre, S. P. Meeker, P. N. Pusey, and W. C. K. Poon, Phys. Rev. Lett. **75**, 958 (1995).
 - [16] J. C. van der Werff, J. Rheol. **33**, 421 (1999).
 - [17] K. N. Pham, A. M. Puertas, J. Bergenholtz, S. U. Egelhaaf, A. Moussa d, P. N. Pusey, A. B. Schofield, M. E. Cates, M. Fuchs, and W. C. K. Poon, Science **296**, 104 (2002).
 - [18] J. Mattsson, H. M. Wyss, A. Fernandez-Nieves, K. Miyazaki, Z. Hu, D. R. Reichman, and D. A. Weitz, Nature **462**, 83 (2009).
 - [19] V. N. Michailidou, G. Petekidis, J. W. Swan, and J. F. Brady, Phys. Rev. Lett. **102**, 068302 (2009).
 - [20] C. Eisenmann, C. Kim, J. Mattsson, and D. A. Weitz, Phys. Rev. Lett. **104**, 035502 (2010).
 - [21] R. J. Larsen, J.-W. Kim, C. F. Zukoski, and D. A. Weitz, Phys. Rev. E **81**, 1 (2010).
 - [22] D. T. N. Chen, Q. Wen, P. A. Janmey, J. C. Crocker, and A. G. Yodh, Annu. Rev. Condens. Matter Phys. **1**, 301 (2010).
 - [23] T. Sentjabrskaja, E. Babaliari, J. Hendricks, M. Laurati, G. Petekidis, and S. U. Egelhaaf, Soft Matter **9**, 4524 (2013).
 - [24] K. J. Mutch, M. Laurati, C. P. Amann, M. Fuchs, and S. U. Egelhaaf, Eur. Phys. J. Spec. Top. **222**, 2803 (2013).
 - [25] T. G. Mason and D. A. Weitz, Phys. Rev. Lett. **75**, 2770 (1995).
 - [26] C. P. Ortiz, R. Riehn, and K. E. Daniels, Soft Matter (2013).
 - [27] R. S. Crandall and R. Williams, Science **198**, 293 (1977).
 - [28] T. Shinohara, T. Yoshiyama, I. S. Sogami, T. Konishi, and N. Ise, Langmuir **17**, 8010 (2001).
 - [29] T. Okubo, H. Ishiki, H. Kimura, M. Chiyoda, and K. Yoshinaga, Colloid Polym. Sci. **280**, 446 (2002).
 - [30] M. Murai, T. Okuzono, M. Yamamoto, A. Toyotama, and J. Yamanaka, J. Colloid Interface Sci. **370**, 39 (2012).
 - [31] H. C. Brinkman, Appl. Sci. Res. **1**, 27 (1949).
 - [32] G. S. Beavers and D. D. Joseph, Journal of Fluid Mechanics **30**, 197 (1967).
 - [33] J. Ochoa-Tapia and S. Whitaker, Int. J. Heat Mass Transf. **38**, 2647 (1995).
 - [34] J. F. Brady, J. Chem. Phys. **99**, 567 (1993).
 - [35] M. Planck, Phys. Zeitschrift **10**, 62 (1909).
 - [36] H. Reiss, H. L. Frisch, and J. L. Lebowitz, J. Chem. Phys. **31**, 369 (1959).
 - [37] A. J. Liu and S. R. Nagel, Annu. Rev. Condens. Matter Phys. **1**, 347 (2010).
 - [38] M. van Hecke, J. Phys. Condens. Matter **22**, 33101 (2010).
 - [39] E. R. Weeks and D. A. Weitz, Phys. Rev. Lett. **89**, 095704 (2002).
 - [40] S. Luding, Physical Review E **63**, 042201 (2001).
 - [41] K. Nichol and K. E. Daniels, Phys. Rev. Lett. **108**, 18001 (2012).
 - [42] D. Acheson, *Elementary Fluid Dynamics* (Clarendon Press, Oxford University Press, New York, Oxford, 1990).
 - [43] P. Carman, Trans. Inst. Chem. Eng. **15**, 150 (1937).
 - [44] N. Darrington et al, Journal of Physics: Condensed Matter **13**, 4891 (2001).
 - [45] S. Ergun and A. Orning, Industrial & Engineering Chemistry **41**, 1179 (1949).
 - [46] J. Kolafa and M. Rottner, Mol. Phys. **104**, 3435 (2006).